Eur. J. Mech. B/Fluids, **17**, n° 4, 489–504, 1998

Structures and transition in a high Reynolds number experiment

H. WILLAIME *, F. BELIN, P. TABELING

ABSTRACT. – We present a brief review of experimental results obtained in high Reynolds number flows using Helium gas as the working fluid. We focus on measurements of the skewness and the flatness of the velocity derivative, and in particular their evolution with the Reynolds number. A transition, observed at $R_\lambda \approx 700$, is discussed. In the second part, we analyze the structures associated with high velocity gradients, which we identify as "worms"; we finally present a detailed analysis of the evolution of their mean size, their number and their velocity increment with Reynolds number. © Elsevier, Paris

1. Introduction

Understanding small scale intermittency appears as a central issue in fully developed turbulence. In the present paper, we review results obtained in the dissipative range of scales and concerning intermittency, we show a study of the probability density functions (pdf) of the velocity derivatives, along with the corresponding skewness and the flatness factors. These results were obtained by using low temperature helium. It turns out that, by using such a fluid, a wide range of Reynolds numbers can be covered, so that it is possible to investigate, in some detail, the variation of such factors with this parameter. While the skewness and flatness factors are found constant in the early Kolmogorov theory, it is well established, both at experimental and numerical levels, that the flatness increases with the Reynolds number. The results we present here, obtained on a particular system, document, in a more detailed way, a range of R_λ lying between 150 and 2000. A transitional behaviour, around a microscale Reynolds number $R_\lambda = 700$, is found. Although so far the existence of a transition has never been reported in other systems, detailed comparison with the best collection of earlier investigations does not reveal any conflict with previous data.

In the second part, we analyze events associated with the highest velocity gradients. We observe a particular family of events that we identify as intense filaments, similar to the "worms" revealed in recent numerical studies (Jiménez *et al.*, 1993) and study their characteristics. A transition, corresponding to that mentioned above, is also found in the evolution of such characteristics with Reynolds number.

Most of the results presented here have already been published in Belin *et al.* (1996), Tabeling *et al.* (1996) and Belin *et al.* (1997): this paper must therefore be considered as a brief review, rather than a report of new results.

2. Experimental set-up

Since the system has been described previously (Zocchi *et al.*, 1994 and Tabeling *et al.*, 1996), we mention here only the main characteristics of the experimental set-up. The flow takes place in a cylindrical vessel, limited axially by two counter-rotating disks. The disks are driven by two independent 28L28 Escap DC-motors,

Laboratoire de Physique Statistique, École Normale Supérieure, 24, rue Lhomond, 75005 Paris, France
* Correspondence and reprints

0997-7546/98/04/© Elsevier, Paris

with rotation speeds ranging from 0.3 Hz to 10 Hz. The dimensions of the cells are: 6.4 cm diameter and 4.8 cm high for the first cell (cell 1) and 20 cm diameter and 13 cm high for the second (cell 2). The system is enclosed in a cylindrical vessel in thermal contact with a liquid helium bath. The working fluid is helium gas. For each experimental run, the pressure and the temperature of the fluid are controlled within 10 mbar and 100 mK respectively.

The local velocity of the flow is measured by hot wire anemometers. The probe is a carbon fiber, covered everywhere except on a spot, by metallic evaporation. The spot defines the sensitive zone, a cylindrical region, 7 μm in length and 7 μm in diameter. The measurements are performed by overheating the sentitive zone, by around 15 Kelvin. The temporal resolution of the probe has been measured by a classic square-wave test and goes up to 50 kHz which makes it possible to resolve all frequencies of the turbulent flow for R_λ up to 2500 and all the inertial range frequencies for R_λ up to 5000. A more detailed discussion concerning the hot wire anemometer is made in Tabeling *et al.* (1996). The signal is recorded on a computer with 16 bit resolution at a frequency rate up to 125 kHz.

Since the kinematic viscotity can be varied by three orders of magnitude by changing the pressure and temperature of the working fluid, it is possible to explore a range of R_λ extending from 150 to 5000. Nonetheless, since at high Reynolds numbers we cease to resolve the dissipative scales, the domain of investigation we consider presently for the study of the dissipative range intermittency is limited to $150 < R_\lambda < 2000$. In Table I, we report typical experimental values.

TABLE I. – Typical experimental values obtained in the 2 cells. R_λ is determined by measuring the dissipation energy using the third order structure function of the velocity.

Cell	ν cm^2/s	U cm/s	u' cm/s	Re	R_λ	u'/U	λ (μm)	η (μm)
2	$1.6\ 10^{-2}$	39	8	41000	151	0.20	3000	127
2	$2.1\ 10^{-2}$	284	94	$2.3\ 10^5$	674	0.33	1520	26
2	$4.6\ 10^{-4}$	128	37	$4.7\ 10^6$	2300	0.29	276	2.9
2	$4.4\ 10^{-4}$	128	27	$5\ 10^6$	1550	0.20	262	3.4
2	$1.1\ 10^{-3}$	64	13	$2\ 10^6$	822	0.21	680	12
1	$2.7\ 10^{-2}$	118	29	16700	188	0.25	1740	64
1	$2.6\ 10^{-4}$	27.4	6.1	$4.3\ 10^5$	879	0.22	187	5

To analyse the turbulent flow, one-point-velocity measurements are performed and the Taylor hypothesis is used to convert time to space.

3. Skewness and flatness of the velocity derivative

Here we summarize observations published in earlier papers (Tabeling *et al.*, 1996; Belin *et al.*, 1997).

The skewness and flatness factors (denoted by S and F respectively) of the longitudinal velocity derivatives are standard diagnostics for dissipative range intermittency and they essentially characterize the tails of the pdfs: they are defined as:

$$S = \langle(\partial u/\partial x)^3\rangle / \langle(\partial u/\partial x)^2\rangle^{3/2}, \quad F = \langle(\partial u/\partial x)^4\rangle / \langle(\partial u/\partial x)^2\rangle^2,$$

in which $u(t)$ is the velocity fluctuation, $x = Ut$ (where U is the local mean velocity and t is time) and the brackets imply a time average (we thus here use the Taylor hypothesis to convert time into space).

The measurement of $-S$ is made by calculating the ratio of $F_3(r)/(F_2(r))^{3/2}$, for arbitrary r, where F_n is the structure function of the velocity of order n. The skewness S is the limit of this ratio as r goes to 0.

The limit is a well-defined plateau when the dissipative scales are resolved (Tabeling *et al.*, 1996). A similar technique is used to measure F.

Figure 1, shows the negative skewness factor $(-S)$ versus the Reynolds number, both for our data and the best compilation to date (Sreenivasan and Antonia, 1997: see also Van Atta *et al.*, 1980, Wyngaard *et al.*, 1970 or Kuo *et al.*, 1971). The plot seems to show a plateau between 20 and 1500 (note that there is a large dispersion of the data, both in the Helium experiment and in the data collected by Sreenivasan *et al.*), while outside this range, it seems that $-S$ increases with the Reynolds number.

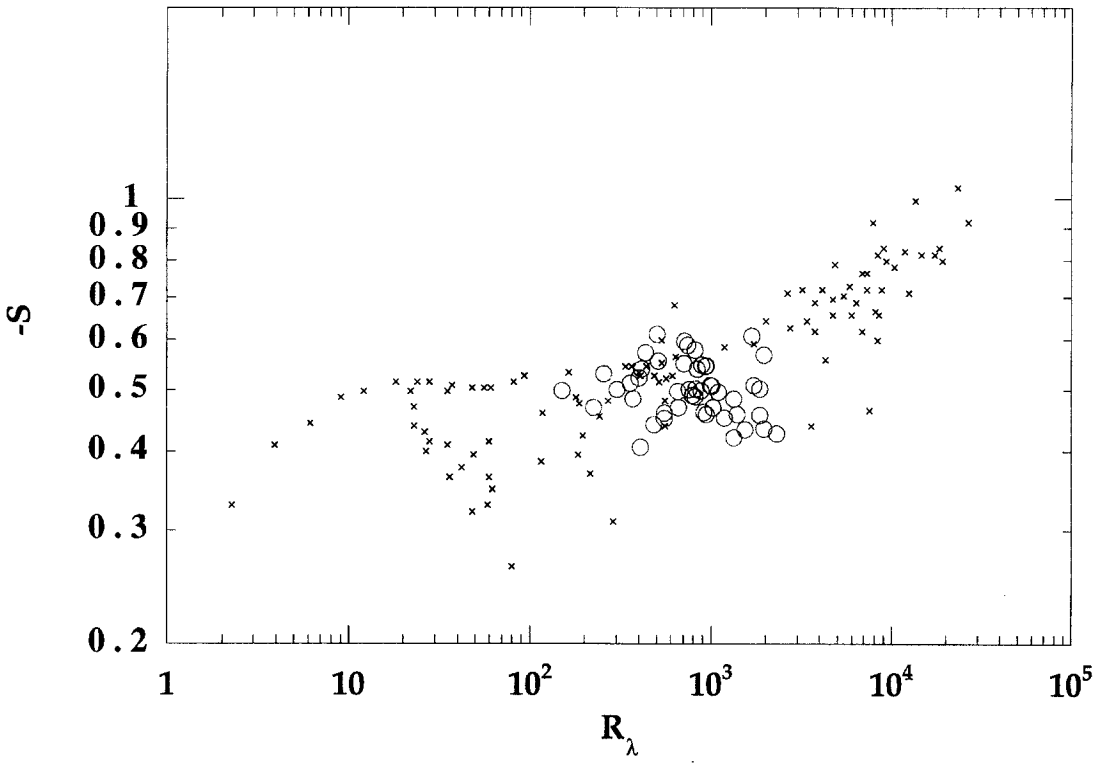

Fig. 1. – Evolution of the skewness as a function of the Reynolds number: ○: results obtained in the helium experinemt, ×: experimental and numerical data from the compilation of Sreenivasan *et al.* (1997).

Concerning the flatness factor F (see *Fig.* 2), a quite complicated evolution takes place for the helium experiment. Below $R_\lambda = 700$ (although 650 might be a more accurate estimate), the flatness increases monotonically with the Reynolds number, signifying that intermittency increases as well. In the range $700 < R_\lambda < 1100$, F decreases until eventually, at higher values of the Reynolds number, F increases again (we obtain a bump in this range of R_λ). It is worth comparing this evolution with existing data. This is shown on Figure 2; there is clearly any conflict between the helium data and the others. It would indeed be instructive to have more measurements using conventional flow geometries in the range where the transition is observed.

One may ask whether the transitional behaviour is due to an artefact. We have performed several checks. For instance, we checked that the measurement is independent of the cell size and of the ratio of the probe size to the Kolmogorov length (Tabeling *et al.*, 1996). We made sure the convergence of the different functions

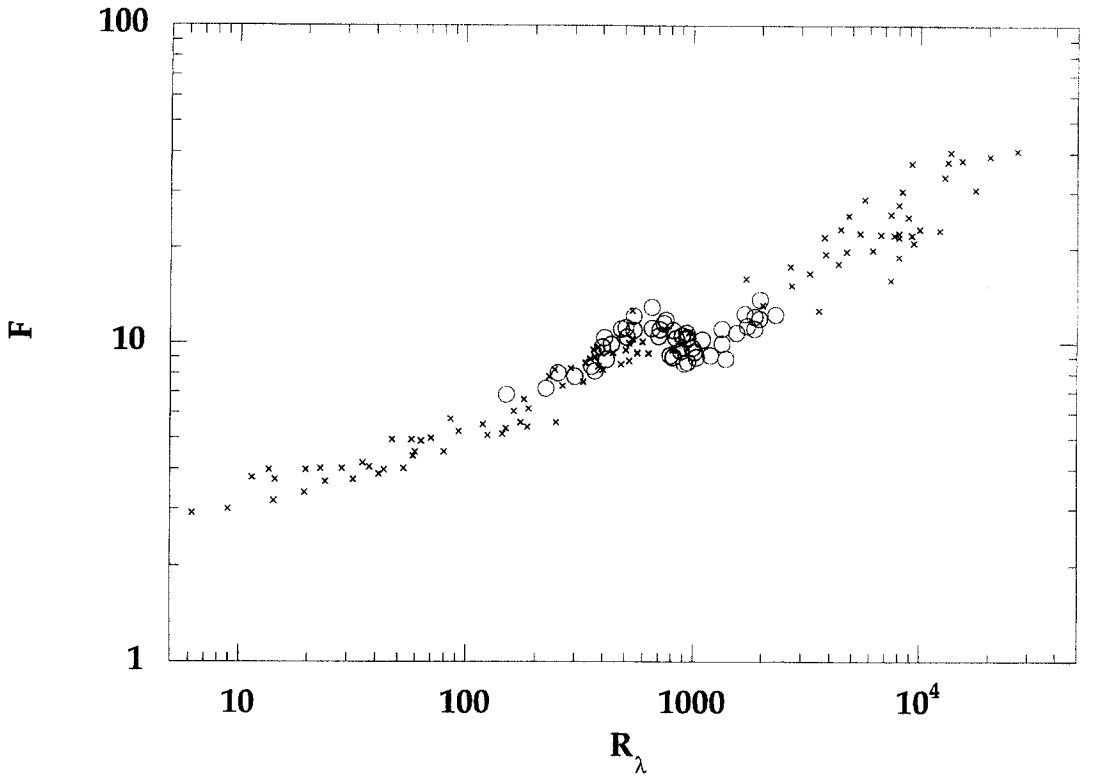

Fig. 2. – Evolution of the flatness as a function of the Reynolds number; same symbols as in Figure 1.

involved in the calculation of the flatness is clearly ensured. Progress was made on the development of the probes: by changing the fixing method of the carbon fiber, we reduced the oscillation of the fiber on its rigide frame and so the corresponding noise. A study made by Emsellem *et al.* (1997) concerning the thermal response of the probe and the vortex shedding behind the probe shows that these two effects probably do not affect the measurements for $R_\lambda < 2000$.

Another issue is whether the transition is specific to the geometry we study. Preliminary results obtained in the same system using corotating disks, and for which the flow is driven over a periodic array of obstacles shows strong indication of the existence of a transition around $R_\lambda = 700$. This suggests that the transition is present in other flow configurations.

Thus we tend to conclude that the presence of an artefact is unlikely, and that the transition should occur in other flow configurations.

4. Worms

4.1. Definition of the objects associated with the largest gradients

Defining objects associated with large gradients, at various Reynolds numbers, raises the delicate question of introducing thresholds which depend on this parameter. To solve this difficulty, we consider the pdfs of the velocity derivatives for various Reynolds numbers, and seek a transform, in terms of this parameter, which makes it possible to collapse the tails of such pdfs onto a single curve. Such a transform has already been

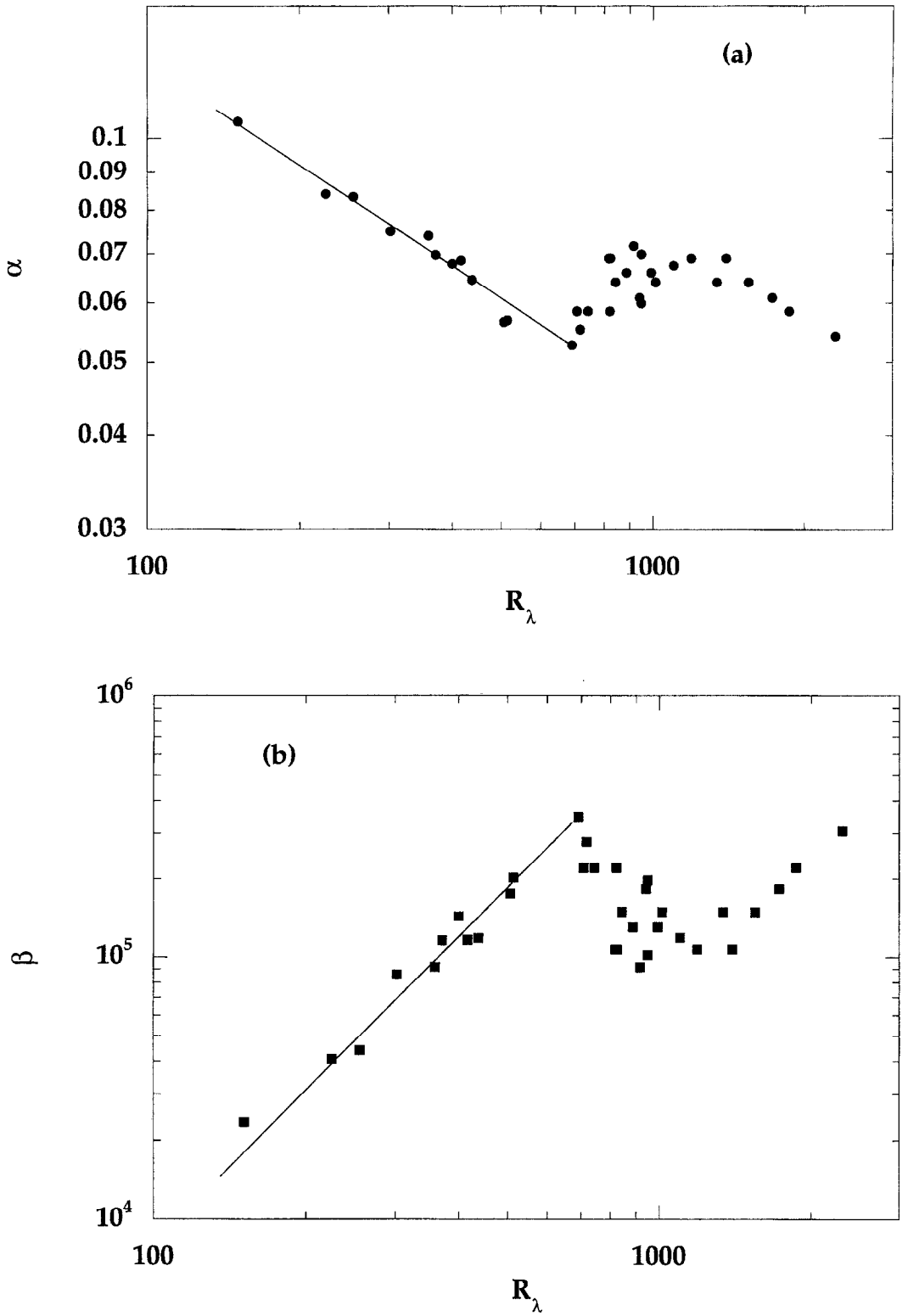

Fig. 3. – (a) Evolution of α as a function of R_λ, the renormalisation factor of the abscissa of the velocity derivative pdfs. (b): Evolution of β, the renormalisation factor of the pdfs.

presented in (Belin *et al.*, 1997). It consists of introducing a set of reduced variables – s^* and p^* – defined by the following relations:

$$s^* = \alpha(R_\lambda)\, s \quad \text{and} \quad p^* = \beta(R_\lambda)\, p,$$

The variable s is defined, as usual, by:

$$s = \frac{\left(\frac{\partial u}{\partial x}\right)}{\left\langle \left(\frac{\partial u}{\partial x}\right)^2 \right\rangle^{1/2}}.$$

The quantity $p(s)$, which is the probability density function for the variable s, has a variance equal to one, by definition; $\alpha(R_\lambda)$ and $\beta(R_\lambda)$ have been introduced previously (Belin *et al.*, 1997), and, for completeness, we show them on Figure 3. Below $R_\lambda = 700$, these quantities follow power laws in the form:

$$\alpha(R_\lambda) = R_\lambda^{-0.5} \quad \text{and} \quad \beta(R_\lambda) = R_\lambda^2.$$

Above 700, the evolution is more complicated. A set of pdf of velocity derivatives, obtained for differnt R_λ, and plotted by using s^* and p^*, instead of the usual s and p as in Belin *et al.* (1997), is shown in Figure 4. One sees that the tails collapse pretty well for $|s^*|$, say, larger than 0.24 (although the limit is not so sharp indeed, whereas below this value, the curves are dispersed. This suggests as a definition for "large gradients" the condition:

(1) $$|s^*| > 0.24$$

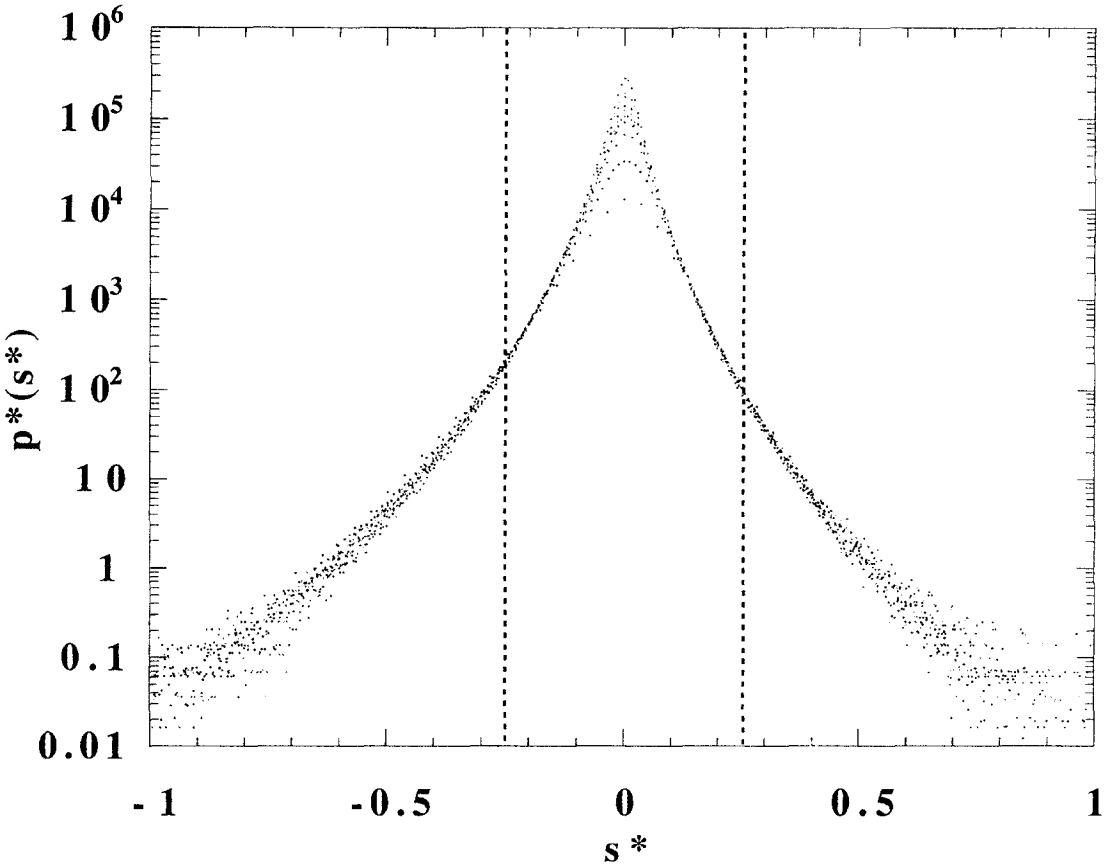

Fig. 4. – Rescaled pdfs of the velocity derivatives for different R_λ (13 different runs at R_λ between 159 and 2313).

for all Reynolds numbers. The threshold used here is a little above that of Belin *et al.* (1996), where a more limited range of values of R_λ was considered. It is consistent with other proposals made in a lower range of R_λ (Jimenez, 1998). The interest of using condition (1) for defining the large gradients, is that the threshold stays at the same place on the tail as R_λ is varied. We will be able to check, in some cases, that the results do not depend critically on the threshold definition.

4.2. Mean shape of the objects composing the tails of the PDF (defined as $s^* > 0.24$)

The produce for determing the mean shape of the objects associated with the largest gradients is as follows: (i) sort out the positive and negative gradients above the threshold defined by $|s^*| > 0.24$, (ii) determine the two local extrema around the gradient, their distance and the peak-to-peak amplitude, (iii) normalize to unity these two quantities, and (iv) calculate the statistical average of the corresponding normalized curves, for each sign.

The result is shown in Figure 5, for the positive and negative signs, and for $R_\lambda = 371$. The averages were performed on a population of 5000 events. The mean shapes look S-shaped and the positive and negative gradients are different. Such an asymmetry indicates the action of vortex stretching, which tends to increase the gradients, at a rate depending on the amplitude of the local velocity fluctuation. The standard deviation around the mean shape is typically 40%, which is sizeable. We have not seen any measurable evolution of the shape with R_λ throughout the range investigated. A similar statement holds for the standard deviation around the mean shape. This reassesses a statement made in Belin *et al.* (1996), which was based on poor statistics.

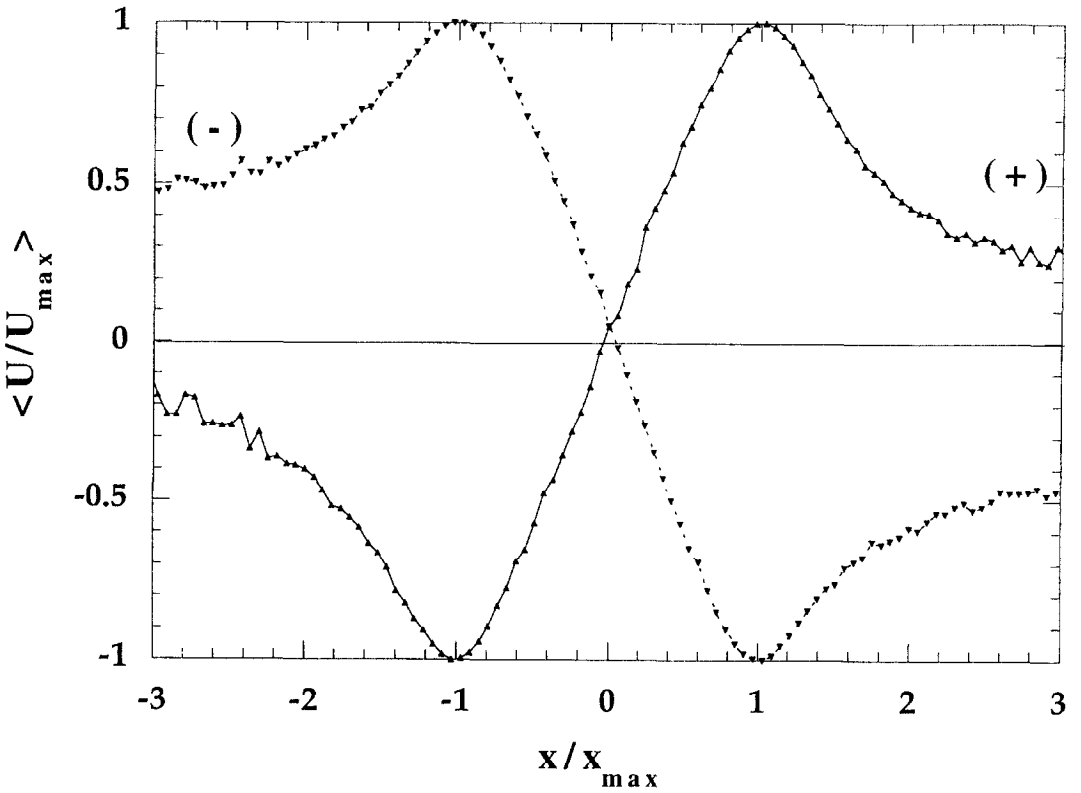

Fig. 5. – Mean shapes of the objects associated with the largest gradients of the system for $R_\lambda = 371$, averaged after amplitude and scale normalization is performed; this normalization is achieved with the maxium velocity $U_{\max}$ and its corresponding position $x_{\max}$. The positive and negative gradients are signalled by (+) and (–) symbols. The brackets represent statistical averaging.

We have attempted to apply the procedure (i)-(iv) to artificially generated signals, so as to appreciate to what extent the shapes of Figure 5 are specific to a given process. Clear differences appear with pure random noise, but shapes similar to those of Figure 5 are obtained with a low pass-band random noise, filtered in a way mimicking the energy spectrum. We concluded, without surprise, that the shape, although conveying interesting and non-trivial information, is not accurately specific of a given process.

4.3. Physical interpretation of the events associated to the large gradients

We use here a physical interpretation previously advanced for the events associated with the large gradients (Belin *et al.*, 1996). The interpretation is based on the hypothesis that such events correspond to the sweeping of isolated Burger filaments onto the probe. The filament is taken normal to the plane defined by the mean flow and the sensor axis, as shown on Figure 6. Its vorticity field is:

$$\omega(r) = \omega_0 \exp\left(-\frac{r^2}{2R^2}\right)$$

in which ω_0 is the core vorticity, and R its radius. In this notation, the worm radius (unfortunately) differs by a factor $\sqrt{2}$ from the usual convention. A useful quantity to be introduced here is the circulation Γ defined by

$$\Gamma = 2\pi R^2 \omega_0$$

The calculation performed in Belin *et al.* (1996) led to the following probe response when the vortex centre hits the probe:

$$S\left(\frac{Ut}{R}\right) = U_\theta(r)\sin\alpha$$

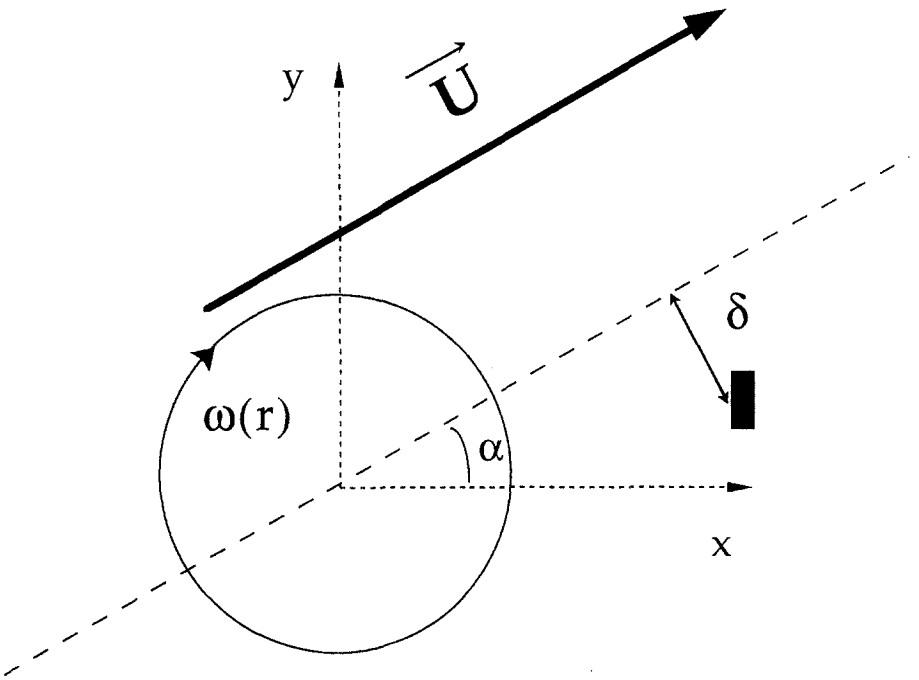

Fig. 6. – Representation of an isolated vortex filament, with its axis normal to the plane (x, y), crossing the hot wire (black rectangle), at a speed U, with an angle α and a distance from vortex center to the probe equal to δ.

in which $U_\theta(r)$ is the velocity induced by the worm, *i.e.*:

$$U_\theta(r) = \frac{\Gamma}{2\pi r}\left(1 - \exp\left(\frac{r^2}{2R^2}\right)\right)$$

where α is the impact angle, *i.e.* the angle between the trajectory of the worm and the axis of the sensor.

In addition, one must also consider that the filaments have an angle and a distance of impact. We have calculated the mean profile $\langle S(t)\rangle$ by selecting only the largest gradients. The result of this calculation gives a profile that agrees fairly well with the experimental curve obtained by averaging the mean profiles of the intense positive gradients (see *Fig.* 7). We may conclude that the average shapes displayed on Figure 5 are likely to correspond to the sweeping of Burger-like vortices onto the probe; as the physical properties of such objects (see below) are comparable to those observed by Jiménez *et al.* (1993), we will call them "worms", even if there is still some uncertainty concerning the nature of such objects.

To be complete, one must also consider worms which are not normal to the plane defined by the mean flow and the sensor axis. This is a delicate problem which was tackled long ago by Kuo and Corrsin (1972) and more recently addressed in Belin *et al.* (1996); one must introduce two additional angles (the pitch and the roll angles) and estimate their influence on the probe response. In practice, it seems enough to introduce correction factors on the distance measurements to account for the fluctuations of those two angles. Dividing by a factor of 1.40 seems a reasonable rule to infer the "true" worm radius (*i.e.* the one obtained if the worm axis was normal to the plane), from the "apparent" one (*i.e.* the one we measure). This rough procedure yields figures consistent with the Kuo and Coorsin estimates (Kuo and Corrsin, 1972).

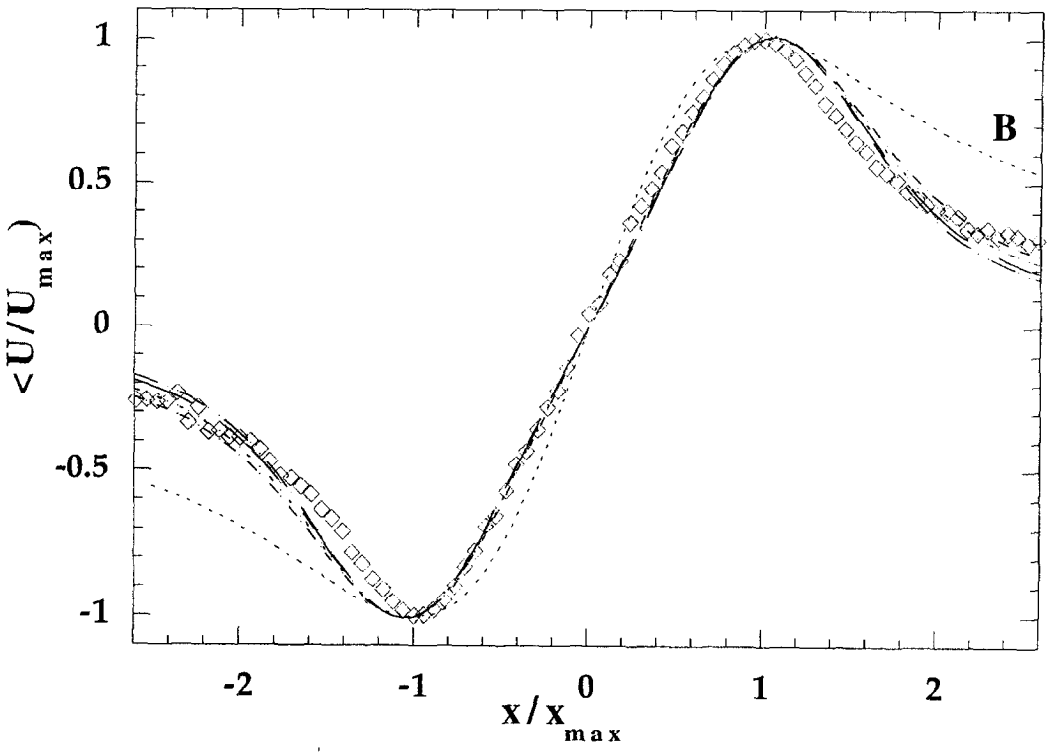

Fig. 7. – Comparison between the average of the mean shapes of the largest gradients for $R_\lambda = 371$, and a statistical average of events produced by Burger type filaments crossing the prove at different impact parameters α and δ, for five fluctuation rates u/U respectively equal to 5, 10, 20 and 30% (they correspond to the set of unalbelled dashed lines). The dashed line labelled by a (B) corresponds to the response generated by an individual Burger vortex, crossing the probe at $\delta = 0$ and small angle.

Eventually, the calculation presented above (along with the incorporation of the factor 1.40) allows a determination of the relation between the worm radius R and the temporal distance Δt between the two extrema located around an intense gradient, and that between the maximal azimuthal velocity U_{mw} and the peak-to-peak amplitude ΔS associated with such extrema. We find the following formula s:

$$R = 0.15\, U\, \Delta t \quad \text{and} \quad U_{mw} = 1.1\, \Delta S \tag{2}$$

from which the worm Reynolds number is:

$$\mathrm{Re}_w = \Gamma/\nu = 2.3\, U\, \Delta t\, \Delta S/\nu \tag{3}$$

The numerical constants in (2) update those previously published in Belin *et al.* (1996), in which the impact parameters were assumed to be fixed and the impact angle small, whereas here those parameters are free to fluctuate over an apprecialby wide range.

4.4. Geometrical characteristics of the worms

The distributions of the worm's size $p\,(R/\eta)$ (where η is the Kolmogorov scale), along with that of the worm's Reynolds number $p\,(U_{mw}/u)$ (where u is, as mentioned previously, the longitudinal turbulent fluctuation), as shown in Figure 8. Figures 8a and 8b are very similar to those published previously (Belin *et al.*, 1996), obtained with a different threshold. They confirm the scaling already proposed, *i.e.* the mean size on the Kolmogorov scale, and the mean velocity increment across them is of the order of the standard deviation of the large scale velocity.

From those distributions, one can extract several quantities of interest. The evolutions of the mean radius, the maximum azimuthal velocity increment and the worms' Reynolds number with R_λ are displayed on Figure 9. Data obtained in numerical studies (Jiménez *et al.*, 1993), and reconverted in our notations, are displayed on the same graph. Both are consistent. One sees that, in our units, the mean radius is three times the Kolmogorov scale up to $R_\lambda = 700$, above which a transitional behavior takes place; the maxium azimuthal velocity is about 0.9 the standard deviation of the turbulent fluctuation below 700, then decreases and perhaps saturates as R_λ is further increased. The worm Reynolds number increases with R_λ, and does not show any transitional behavior. A best fit procedure yields an exponent 0.40 ± 0.1 for Re_w, which is consistent with the value 1/2 that we expect.

An interesting plot for checking the consistency of the analysis is the sensititivy of the mean radius R, and the mean worm Reynolds number Re_w to the threshold values of s^* taken for the worm definition. The evolutions of R, and Re_w with s^* are shown on Figure 10, for $R_\lambda = 225$. Both quantities tend (albeit roughly) to saturate as s^* is increased above 0.2-0.3. It is thus reasonable to define a region in the distributions of the velocity derivatives, where intrinsic characteristics can be sought. By contrast, below 0.20, the measurements are sensitively dependent on the threshold.

4.5. Contribution of the worms to the statistical characteristics of the flow

It is interesting to evaluate the contribution of the worms in the system. In a previous paper we have studied, for a specific case, the influence of such structures on some statistical quantities (the effect on the pdf of velocity increment, on structure function exponents and on energy spectrum, *see* Belin *et al.*, 1996). We have shown in particular the following: "worms" are objects that control the tails of the pdf of the velocity derivative and contribute to the intermittency shown in the inertial range. Without "worms" the flow is less intermittent. Here we complete the previous study by analysing this contribution as a function of the Reynolds number.

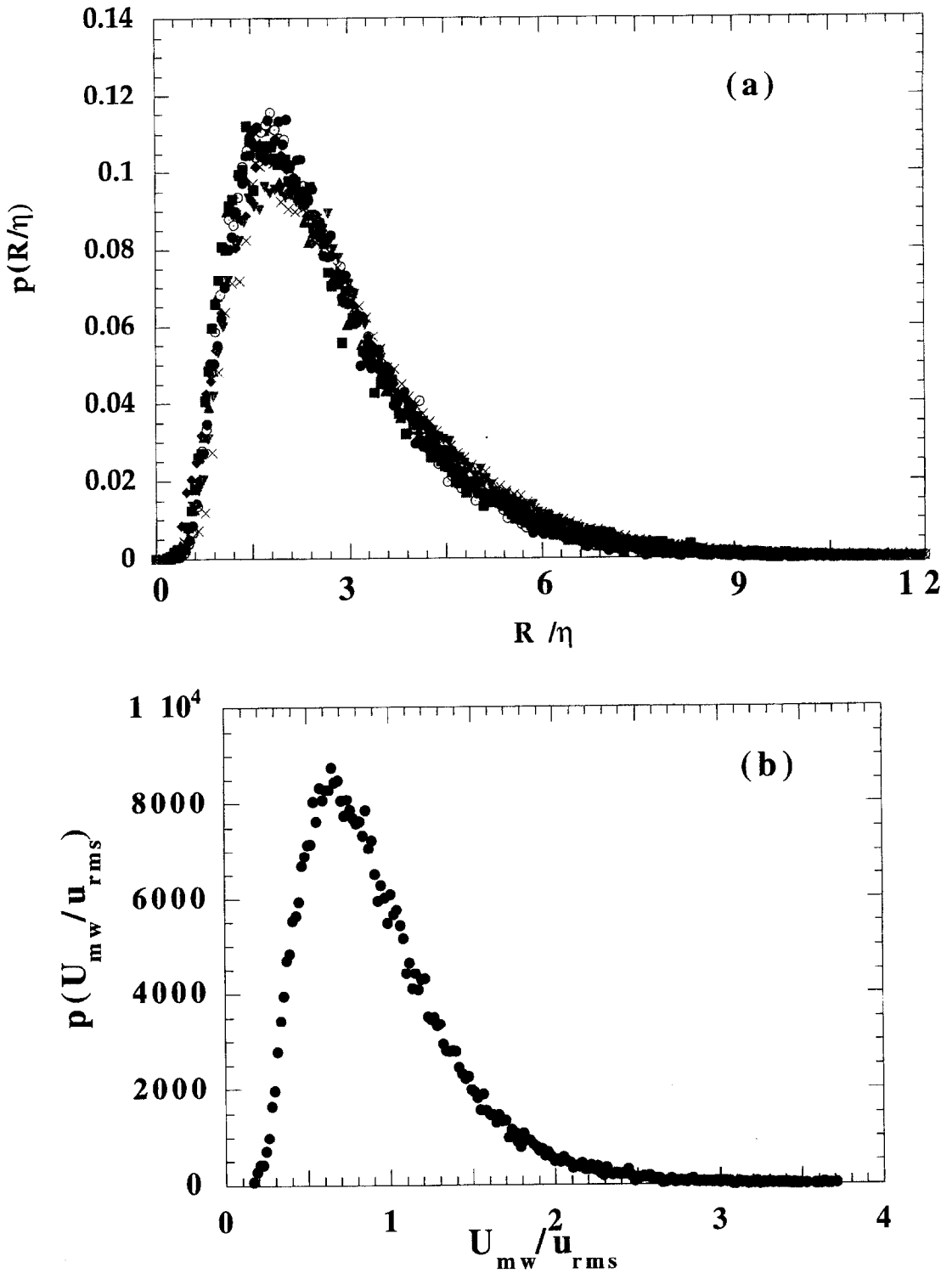

Fig. 8. – Distribution of worm radius R and maximum worm velocity U_{mW}, (a) using linear scales, and Kolmogorov units, for 13 various different R_λ between 150 and 700 (b) velocity increment distribution, on linear scales, for $R_\lambda = 438$. Note that in the case (a) the ordinate is rescaled so as the optimize collapse.

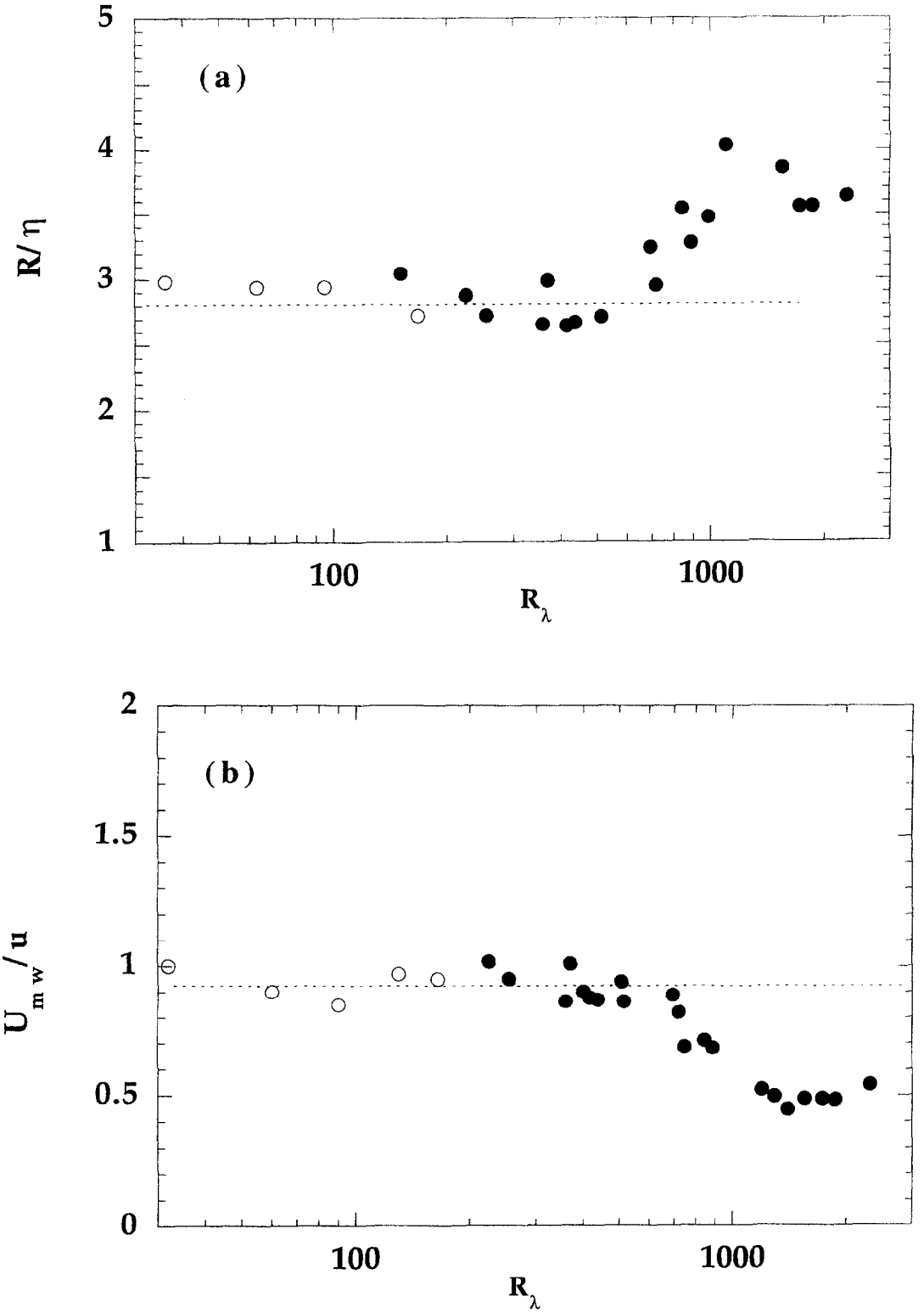

Fig. 9. – (a), (b).

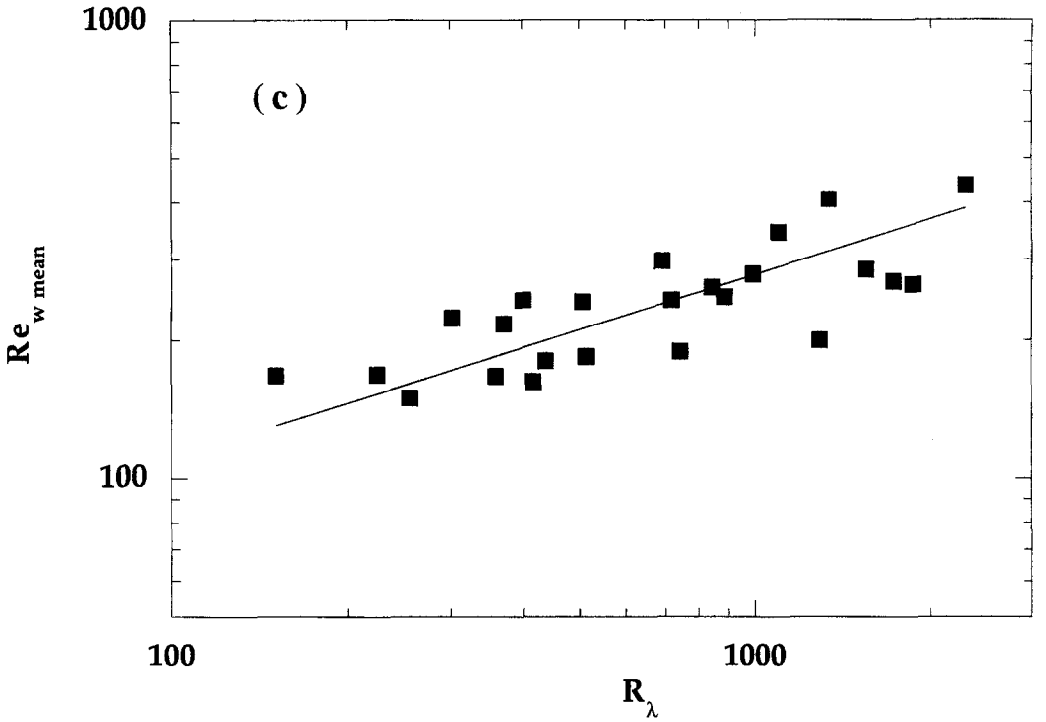

Fig. 9. – (a) Variation of the ratio R/η with R_λ, (b) Variations of the ratio U_{mw}/u with R_λ, (c) Variation of Re_w with R_λ using formula (3); The circles are data obtained by Jiménez *et al.* (1993) and the black disks correspond to the present work; the dashed lines helps to localize the region where no evolution is visible, and the full ine on Figure (c) is a best fit, yielding an exponent equal to 0.40 ± 0.1.

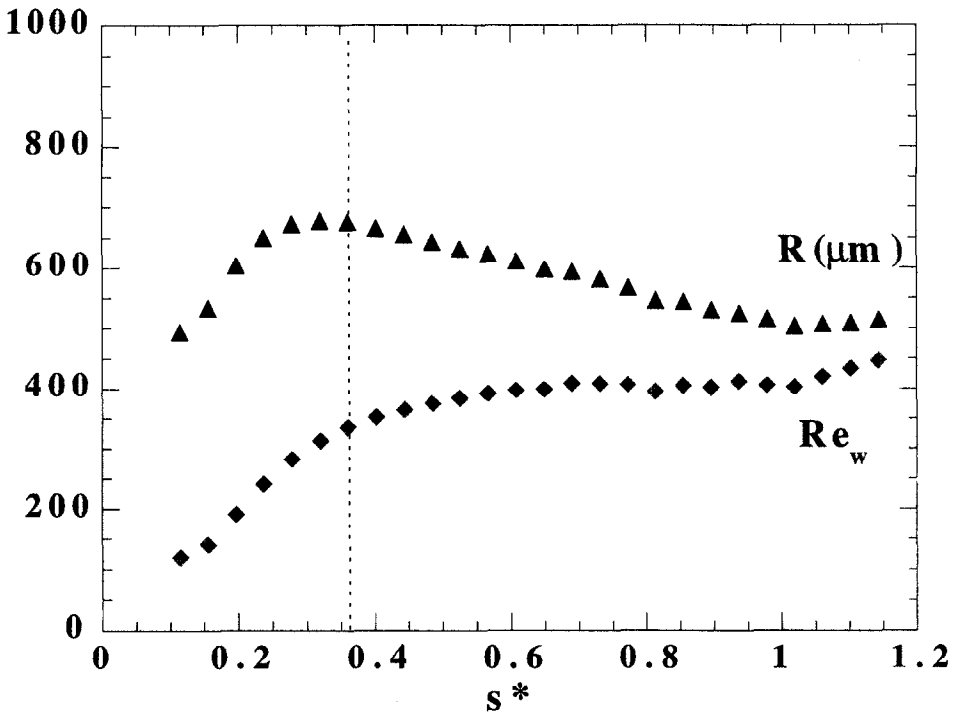

Fig. 10. – Evolution of R_{mean} and $\mathrm{Re}_{\mathrm{wmean}}$ with the threshold s^* used for the definition of the worms, for $R_\lambda = 225$.

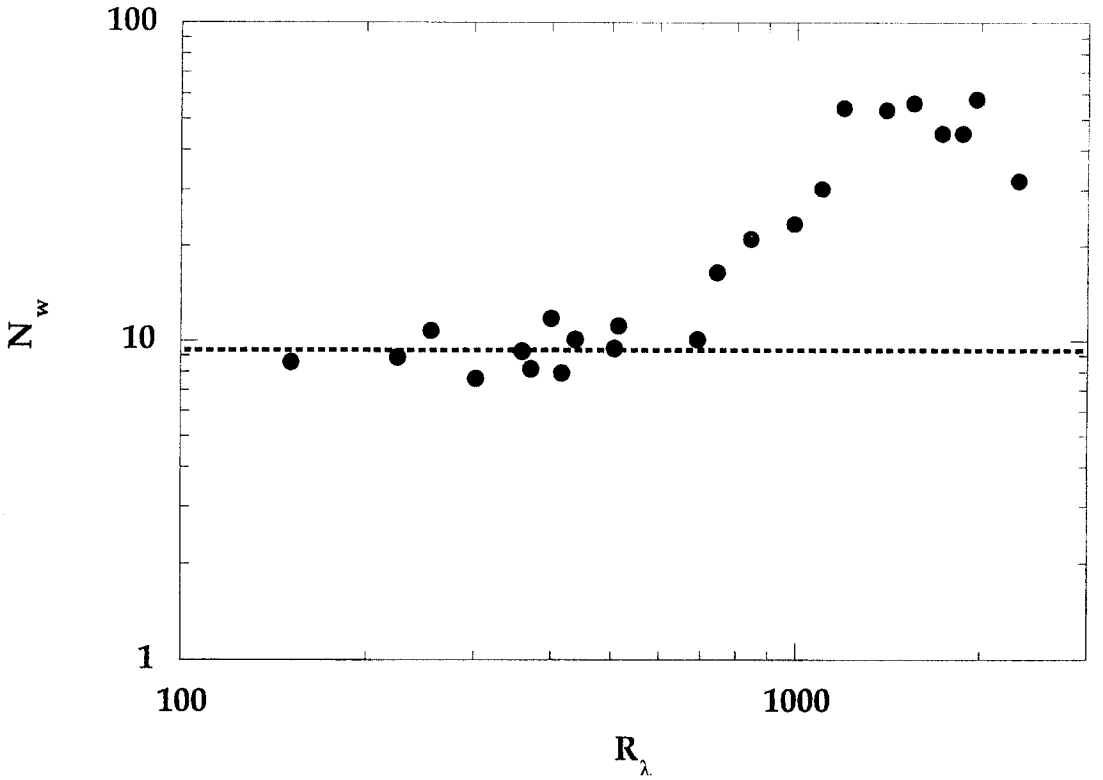

Fig. 11. – Evolution of the number N of worms that cross the probe in one disk rotation as a function of R_λ.

To perform this analysis, the worms (together with their immediate neighbourhood, over up to three times the radius), are removed from the time recordings and replaced by straight lines ensuring the continuity of the signal. This study is performed for R_λ below 650. We analyze here the influence of the worms on the exponents of the strucure functions, for various Reynolds numbers.

An interesting point is first the evolution of the number of worms that cross the probe in one disk rotation. One again finds two regimes (*Fig.* 11). For low Reynolds numbers, the number of worms per unit of integral time N is a constant, while this number increases by up to a factor of 5 between $R_\lambda = 600$ and 1300. For higher R_λ, N is again constant.

Figure 12, shows the relative amount of signal we remove and the corresponding effect on the structure function exponents (therefore, we define the ratio of intermittency removed in the sense of the structure function exponents: $r = (\zeta'_p - \zeta_p)/(p/3 - \zeta_p)$ where ζ_p is the exponent of the structure function of order p for the signal with the worms and ζ'_p without worms). At low Reynolds numbers ($R_\lambda = 151$), 25% of the signal is removed and this decreases down to 1.6% at the highest R_λ we consider. It is not surprising to see that the volume occupied by the worms decrease with the Reynolds number (their number is constant whereas the mean radius decreases as the Kolmogorov scale). This probably explains that the influence of the worms on the structure function exponents in the inertial range decreases with the Reynolds number, as shown on Figure 12.

For $R_\lambda = 151$, the worms seem to control the deviations from Kolmogorov ($r = 100\%$) while for higher Reynolds number, their influence is rather weak (down to 18%). One may wonder whether the importance of the worms at low Reynolds number is because, in such a range, the difference between dissipative and inertial range properties tends to be blurred.

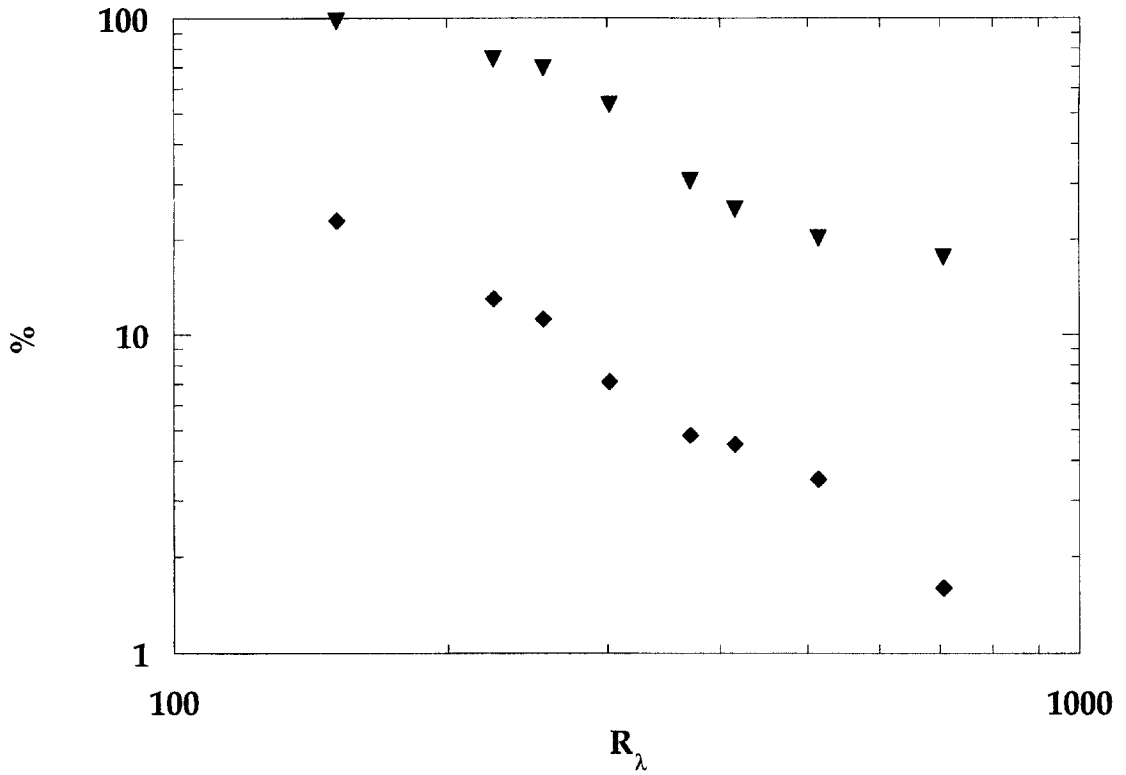

Fig. 12. – ♦: relative amount of signal removed. ▼: ratio of intermittency removed as seen by inspecting the structure function exponents.

5. Conclusion

In conclusion, we have shown that there exists a transitional behaviour in our system. Above a critical value $R_\lambda \sim 700$ the flatness of the velocity derivative decreases with the Reynolds number, while above $R_\lambda \sim 1100$, the flatness increases again. This transition does not conflict with other investigations.

We also identify structures linked to high velocity gradient events, which we call worms. Such structures have also been observed recently in a wind tunnel experiment with a two component velocity signal (longitudinal and transversal velocity, Malecot and Gagne, 1997). In the present helium experiment, these structures undergo a transition as the Reynolds number is increased above 700. Before the transition, their density, their mean size (rescaled by the Kolmogorov scale) and the corresponding velocity increments (rescaled by u_{rms}) are constant whereas above the transition, these quantities vary with the Reynolds number. Beyond $R_\lambda = 1300$ they eventually become constant again, but at different levels. In the transitional zone (*i.e.* between $R_\lambda = 650$ and $R_\lambda = 1300$), the population increases by a factor of 5. On physical grounds, it is quite surprising that just above the transition, the numbers of worms increases. One may speculate whether this signals the onset of a new type of filament, which might be called "micro-worms"; we may suggest that these objects are produced by the instability of the worms. This would be the next step in a cascade. Amazingly, such objects would violate the frozen turbulence hypothesis, which would therefore raise new, unexpected, issues.

Acknowledgements. – The authors would like to thank Olivier Cardoso for his continuous and needful help concerning the acquisition systems, J. Jimenez, O. Cadot, S. Douady and Y. Couder for interesting discussions concerning the experiment. Special thanks to K. Streenivasan for permission to use the data from his review

paper. The authors are grateful to the Portescap (Switzerland) who supply grease-less motors for low temperature use. This work was supported by the Ecole Normale Supérieure, CNRS, Universities Paris VI and VII.

REFERENCES

BELIN F., MAURER J., TABELING P., WILLAIME H., 1996, Observation of Intense Filaments of Fully Developed Turbulence, *J. Phys. II*, **6**, 573-583.

BELIN F., MAURER J., WILLAIME H., TABELING P., 1997, Velocity gradient distributions in fully developed turbulence: An experimental study, *Phys Fluids*, **9**, 3843-3850.

CADOT O., DOUADY S., COUDER Y., 1995, Characterization of the low-pressure filaments in a three-dimensional turbulent shear flow, *Phys. Fluids*, **7**, 630-646.

EMSELLEM V., KADANOFF L. P., LOHSE D., TABELING P., WANG Z. J., 1997, Transition and probes in turbulent helium, *Phys. Rev. E.*, **55**, 2672-2679.

JIMÉNEZ J., WRAY A. A., SAFFMAN P. G., ROGALLO R. S., 1993, The structures of intense vorticity in isotropic turbulence, *J. Fluid. Mech.*, **255**, 65-90.

JIMÉNEZ J., 1998, Small scale intermittency in turbulence, This volume.

KERR R. M., 1985, Higher order derivative correlations and the alignment of small-scale structures in isotropic numerical turbulence, *J. Fluid. Mech.*, **153**, 31-58.

KUO A., CORRSIN S., 1971, Experiments on internal intermittency and fine-structure distribution functions in fully turbulent fluid, *J. Fluid Mech.*, **50**, 285-320.

KUO A., CORRSIN S., 1972, Experiment on the geometry of the fine-structure regions in fully turbulent fluid, *J. Fluid Mech.*, **56**, 447-479.

MALECOT Y., GAGNE Y., 1997: private communication.

SIGGIA E. D., 1981, Numerical study of small-scale intermittency in three-dimensional turbulence, *J. Fluid Mech.*, **107**, 375-406.

SREENIVASAN K. R., ANTONIA R. A., 1997, The phenomenology of small-scale turbulence, *Ann. Rev. Fluid Mech.*, **29**, 435-472.

TABELING P., ZOCCHI G., BELIN F., MAURER J., WILLAIME H., 1996, Probability density functions, skweness, and flatness in large Reynolds number turbulence, *Phys. Rev. E*, **53**, 1613-1621.

VAN ATTA C. W., Antonia R. A., 1980, Reynolds number dependence of skewness and flatness factors of turbulent velocity derivatives, *Phys. Fluids*, **23**, 252-257.

WYNGAARD J. C., TENNEKES J. L., 1970, Measurements of the small-scale structure of turbulence at moderate Reynolds number, *Phys. of Fluids*, **13**, 1962-1969.

ZOCCHI G., TABELING P., MAURER J., WILLAIME H., 1994, Measurement of the scaling of the dissipation at high Reynolds numbers, *Phys. Rev. E*, **50**, 3693-3700.

(Received 30 July 1997,
revised 10 March 1998,
accepted 19 March 1998)